Normalized Microwave Reflection Index: A Vegetation Measurement Derived From GPS Networks

Kristine M. Larson and Eric E. Small

***Abstract*—Measurements of vegetation state are required both for modeling and satellite validation. Reflected GPS signals recorded by the Plate Boundary Observatory network provide a source of new information about vegetation state in the western United States and Alaska. The GPS ground stations were installed between 2005 and 2008 to measure plate boundary deformation. They operate continuously and transmit their data to a public facility at least once per day. However, they also act as bi-static radars by recording the interference between a direct GPS signal (transmitted at 1.5 GHz) and a reflected GPS signal. The frequency of this interference pattern primarily depends on the vertical distance between the antenna and the ground reflector. As an L-band sensor, the amplitude of the interference pattern depends on vegetation water content. A daily vegetation metric that depends on reflection amplitudes, Normalized Microwave Reflection Index (NMRI), is defined. A method for removing outliers caused by snow and rain is described. The footprint of NMRI depends on the antenna height and local terrain. The minimum footprint is $1000\ \mathrm{m}^2$. A database of more than 300 station NMRI time series has been compiled; these data span the period from 2007 to 2012. Comparisons between NMRI and in situ sampling of vegetation state are the subject of a companion paper.**

***Index Terms*—Geodesy, global positioning system, reflectometry, vegetation mapping.**

I. Introduction

THE amount of water stored in vegetation canopies is an important biophysical parameter for both climate studies and drought monitoring. For example, the productivity of natural and agricultural ecosystems is strongly controlled by plant water status [1]. Knowledge of the amount of biomass and its water content can guide fire management practices [2]. Quantifying the amount of water in plants is also critical for retrieval of hydrologic variables from remote sensing data—as both passive and active remote sensing of soil moisture requires knowledge of vegetation water content (VWC) [3], [4]. Accordingly, remote sensing methods have been developed to estimate water in vegetation, using both optical and radar data.

There is a long history of using optical remote sensing to estimate biophysical parameters. The Normalized Difference Vegetation Index (NDVI) [5], and similar indices [6], has been calculated from operational satellite data for decades. NDVI is largely considered as a measure of plant greenness, and has been used to infer biomass, Leaf Area Index (LAI), fractional vegetation cover, and other variables [7]–[9]. VWC has also been estimated from NDVI, although a cause–effect relationship does not exist between the two variables [10]. Factors such as plant type, plant–water status, and hydroclimatic conditions affect VWC and "greenness" differently, thus the relationship between NDVI and VWC is not expected to be strong [11].

An optical remote sensing index to more directly quantify the amount of water in vegetation is known as Normalized Difference Water Index (NDWI) [12]. It is calculated using reflectance in two near infrared (NIR) channels. Similar indices have been proposed that use reflectance at other NIR wavelengths, either tuned for different satellite channels or to capitalize on other water absorption bands [2], [13]–[15], [10]. Validation of these indices by comparison to *in situ* observations demonstrates a range of performance, depending upon vegetation type, sensor configuration, and other factors. Reflection from the underlying soil complicates the use of NDWI and related indices in areas with fractional vegetation cover or low LAI [12], [13], [10].

Both passive and active microwave remote sensing have been used to estimate water stored in vegetation [16]. The dielectric constant of water is roughly ten times higher than for dry vegetation. Therefore, the amount of water stored in plant material directly affects how microwave radiation interacts with vegetation canopies, including changes in scattering, polarization, and absorption. The amount of water in vegetation affects the emissivity of the canopy, and thus the brightness temperature sensed remotely [17]. Water in vegetation also absorbs microwave radiation emitted by the soil surface, thus VWC hinders retrieval of soil moisture via passive radar sensing [3]. Vegetation optical depth (VOD) can be retrieved from brightness temperature measurements. Comparisons between the seasonal evolution of VOD and NDVI show that there are both similarities and differences between these microwave and optical measures [18].

Active microwave experiments have shown that VWC and other biophysical parameters affect the scattering coefficient and polarization of signals from vegetation canopies. Various sensor configurations have been evaluated, including a range of wavelengths, polarizations, and incidence angles [19]–[22]. In general, the scattering coefficient increases as VWC and biomass increase, with the greatest sensitivity at incidence angles of $\sim 20^\circ - 40^\circ$ off nadir. At L-band, radar backscatter is sensitive across a wide range of VWC ($0 - 5\ \mathrm{kg/m}^2$) [23]. L-band signals penetrate all but the thickest vegetation canopies (e.g., tropical forests), and therefore they are also affected by soil moisture [4]. In addition to soil

Manuscript received June 09, 2013; revised October 22, 2013; accepted January 06, 2014. This research was supported in part by EAR-0948957, AGS-0935725, EAR-1144221, and NNX12AK21G.

K. M. Larson is with the Department of Aerospace Engineering Sciences, University of Colorado, Boulder, CO 80309 USA (e-mail: Kristinem.larson@gmail.com).

E. E. Small is with the Department of Geological Sciences, University of Colorado, Boulder, CO 80309 USA.

Color versions of one or more of the figures in this paper are available online at http://ieeexplore.ieee.org.

Digital Object Identifier 10.1109/JSTARS.2014.2300116

moisture, the VWC-backscatter relationship is complicated by vegetation structure and soil surface roughness. The influence of these factors may be minimized by using the Radar Vegetation Index (RVI), which incorporates both cross- and co-polarized measurements [23], [24].

A relatively new L-band remote sensing technique with relevance for measuring vegetation state uses reflected GPS [and more generally GNSS (Global Navigation Satellite Systems) signals]. Reflected GPS signals were first proposed in 1993 as a method to measure sea level from space [25]. This idea has since been expanded and tested on a variety of ground, aircraft, and space-based platforms for studies of soil moisture [26], [27], altimetry [28], [29], ocean winds [30], sea ice [31], oil slicks [32], ocean tides [33], [34], and snow [35]. Most relevant to this study are the GPS reflection studies of [36]–[38], where the technique is applied to vegetation. These investigators showed that GPS signal power levels could be used to detect vegetation changes for a variety of agricultural crops, including corn, sorghum, wheat, barley, sunflowers, and leaves in walnut trees. Good agreement was shown between the GPS retrievals and field observations of vegetation height and VWC.

In this paper, we describe an alternative way to use GPS to measure VWC. An index is derived from these data, Normalized Microwave Reflection Index (NMRI). As with [36]–[38], a bistatic-radar geometry is used. L-band signals transmitted by GPS satellites are reflected by the land surface and received by geodetic-quality GPS antennas a few meters above the ground. A limited number of comparisons between these types of GPS reflections and *in situ* observations of plant biophysical parameters were first presented by [39]; they also compared time series of GPS reflections and NDVI from several sites in the western United States. In this paper, we summarize the theory that explains the reflected GPS signals, present a method to quantify reflections from the GPS observations, describe the data editing required for a useful metric, and provide a first-order normalization to correct for terrain effects. Validation of the NMRI method by comparison with *in situ* measurements of VWC is covered in a companion paper ([40], hereafter paper II).

II. Overview of the Global Positioning System

NMRI is based on reflection effects recorded in GPS ranging data, known as pseudoranges and carrier phases. The goal of this section is to first provide a description of the GPS system needed to define NMRI. This will be followed by a theoretical description of multipath geometry and how it can be observed in GPS measurements known as pseudoranges.

A. Satellites

GPS is a constellation of satellites (currently 31) at an altitude of $\sim 20\,000$ km above the surface of the Earth. Each GPS satellite orbits the Earth with a ~ 12 h orbital period, meaning that the ground tracks repeat at a nearly sidereal (23 h:56 min) period [41]. The satellites are separated into six orbital planes spaced at 60° intervals and inclined at an angle of 55° with respect to the equator. As a result, GPS receivers in the continental U.S. can track anywhere from 6 to 12 GPS satellite signals

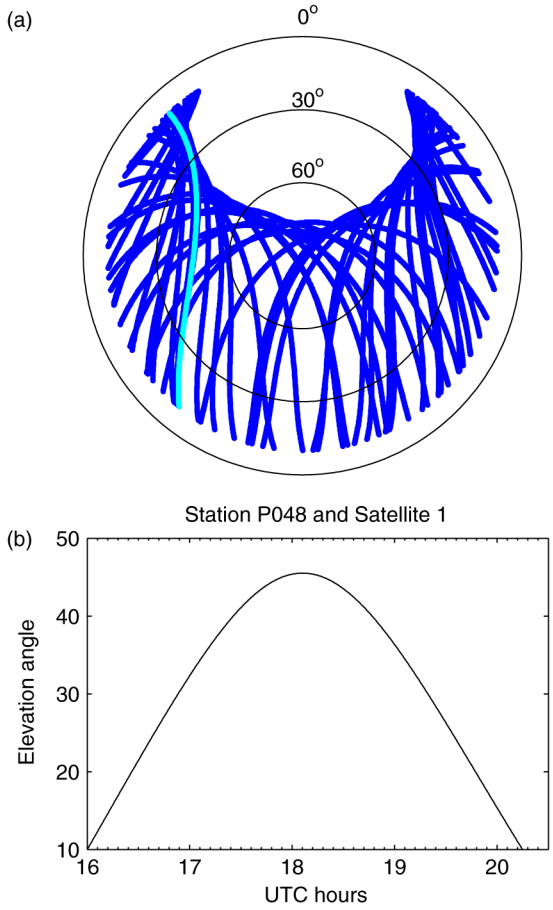

Fig. 1. (a) Polar plot representation of satellite azimuth and elevation angles for PBO site P048, located in southern Montana. Concentric circles represent satellite elevation angles (the angle with respect to the horizon). North is the top of the plot, east is to the right, etc. Note that there are no GPS satellite tracks to the north. The track for satellite 1 is highlighted in cyan and (b) time versus elevation angle for satellite 1.

at any given time. All GPS satellites transmit right-handed circularly polarized (RHCP) signals at L-band. The primary GPS transmission frequencies (f_1 for the L_1 band and f_2 for the L_2 band) are 1.57542 and 1.22760 GHz; the equivalent L_1 and L_2 carrier wavelengths λ_1 and λ_2 are approximately 0.19 and 0.244 m.

The geometry of these GPS satellite tracks strongly depends on the receiver's latitude. Fig. 1 displays the azimuth and elevation angle of all visible GPS satellites for a site located in southern Montana. (Elevation is the angle of the satellite with respect to the local horizon.) No observations are shown below 10° for reasons that will be discussed in Section III. While individual satellite tracks vary, the satellite highlighted in Fig. 1(a) takes approximately 4 h to rise and set, reaching a maximum elevation angle of $\sim 45^\circ$ [Fig. 1(b)]. Longer satellite tracks—that reach higher elevation angles—generally correspond to ~ 6 h in the western United States.

In North America, there is a distinctive hole in GPS observations to the north, which is due to the inclination of the GPS orbit; there is an equivalent measurement hole in the south for GPS users in the southern hemisphere. Depending on which satellites are in which orbital planes and the user's location, a stationary GPS receiver will track a given GPS satellite once or twice per

day. The location of GPS satellites within their orbital planes has varied somewhat over the past 6 years, but not in a way that significantly impacts the footprint of the GPS reflections.

B. Ground Networks

Starting in the mid-1980s, geodesists and geophysicists demonstrated that dual-frequency carrier-phase GPS instruments could be used to measure fault motions [42]. However, the cost of such receivers was prohibitive for permanent installations. As the price of GPS instrumentation decreased in the 1990s, geophysicists began deploying continuously operating GPS instruments. Data from these networks are typically downloaded once per day and made immediately available via the internet.

More than 3000 geodetic-quality GPS sites are currently operating in the United States. Many of these are operated by individual city, county, and state agencies. These GPS sites primarily support precise surveying activities; others are operated by the U.S. Geological Survey to support hazard studies for earthquakes and volcanoes. Universities have augmented these networks to study specific faults. In this study, we use GPS data from the NSF EarthScope Plate Boundary Observatory (PBO) (Fig. 2). The locations of the PBO sites were chosen to facilitate scientific investigations of tectonic signals. Thus, there are a very large number of sites that follow the general outline of the San Andreas Fault in California. Likewise, there are receivers across the Basin and Range that trend east to west because the fault zones in this area are oriented north-south. Clusters of instruments can also be seen at Yellowstone, Mt. St. Helens, and Mammoth Volcanoes. Although a large number of sites are located in urban areas, particularly near Los Angeles, over 90% are situated in natural environments. There are a total of 1100 GPS sites in the PBO network (see http://pbo.unavco.org for a current listing).

The GPS instrumentation at each PBO site is nearly identical (Fig. 3). The GPS receivers (the Trimble NetRS model) can track up to 12 GPS satellites at a time. The antenna is covered by an acrylic dome; the latter provides protection from the snow, leaves, dirt, etc. This "choke-ring" antenna is designed to preferentially receive RHCP signals from above the horizon, i.e., elevation angles greater than zero [43]. Most of the antennas deployed by PBO were mounted on a 2-m tall tripod that was drilled into bedrock. Standard data retrievals are every 15 s. While consistent receiver/antenna units were used at each site, the terrain at each site does vary significantly. The digital elevation map for a representative GPS site (P048) is also provided in Fig. 3.

The PBO network was built between 2005 and 2008. Those initial years were valuable for identifying problems with the GPS hardware, telemetry, and receiver firmware. By late 2006, most of these issues had been resolved. The database described in this study begins on January 1, 2007 and extends through the end of 2012.

III. GPS Multipath: Theory

In order to estimate position, GPS units measure biased distances (ranges) from multiple satellites to the receiving antenna, measurements called pseudoranges and carrier phases. As

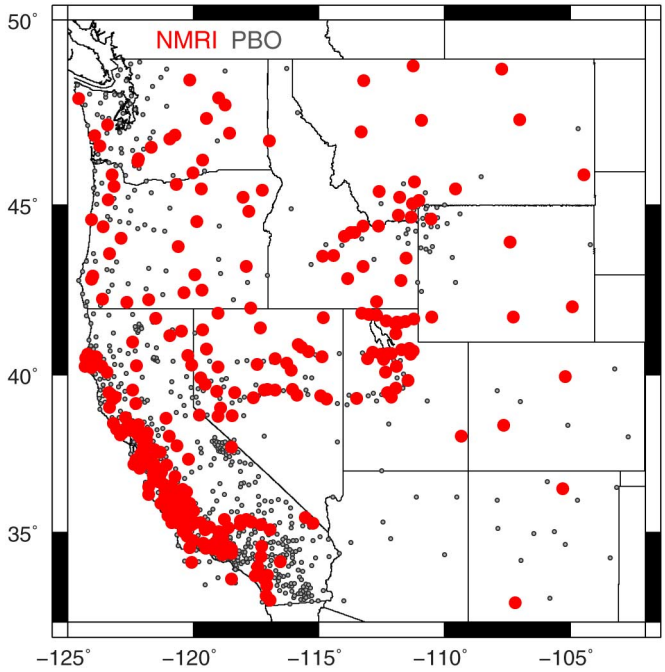

Fig. 2. Locations of GPS sites in the PBO are shown in gray. The sites with currently available NMRI time series are highlighted in red. An additional 150 PBO sites are in Alaska (30 NMRI sites).

a GPS antenna must be able to track multiple satellites from different directions in the sky, an "omni-directional" antenna is used. It is difficult to design an antenna that rejects all energy from reflected signals (i.e., those arriving from negative elevation angles) without negatively impacting the direct signals that arrive from positive elevation angles. The antenna used by geodesists is a compromise. The gain pattern is fairly homogeneous, which is important to geodesists because they want each antenna to have the same geometric phase center location. The antenna gain pattern was designed to strongly prefer RHCP over LHCP measurements so that direct signals (RHCP) would dominate over reflected signals (LHCP). For elevation angles above $\sim 25^\circ$ and natural surfaces such as soil and snow, this antenna design is adequate. However, its efficiency breaks down at lower elevation angles for two reasons:

1) The antenna RHCP gains are nearly equal for positive and negative elevation angles.
2) Reflections from most natural land surfaces retain the polarization of the incident vector electric field in the limit of grazing incidence.

For example, the Brewster angle is $10^\circ - 25^\circ$ for bare soil, depending on whether it is wet or dry. This is far different than what would be observed, e.g., if the GPS antenna were deployed over a large metal surface such as copper. In this case, the reflected energy at low elevation angles would be LHCP and would be rejected by the antenna.

In addition to issues related to the antenna, reflected GPS signals are defined by their geometry (Fig. 4). The GPS antenna receives both direct and reflected energy and the receiver measures the interference between them. To characterize the behavior of this "GPS interferometer," we need to know the wavelength of the carrier signal and how well the two signals are synchronized (i.e., its phase).

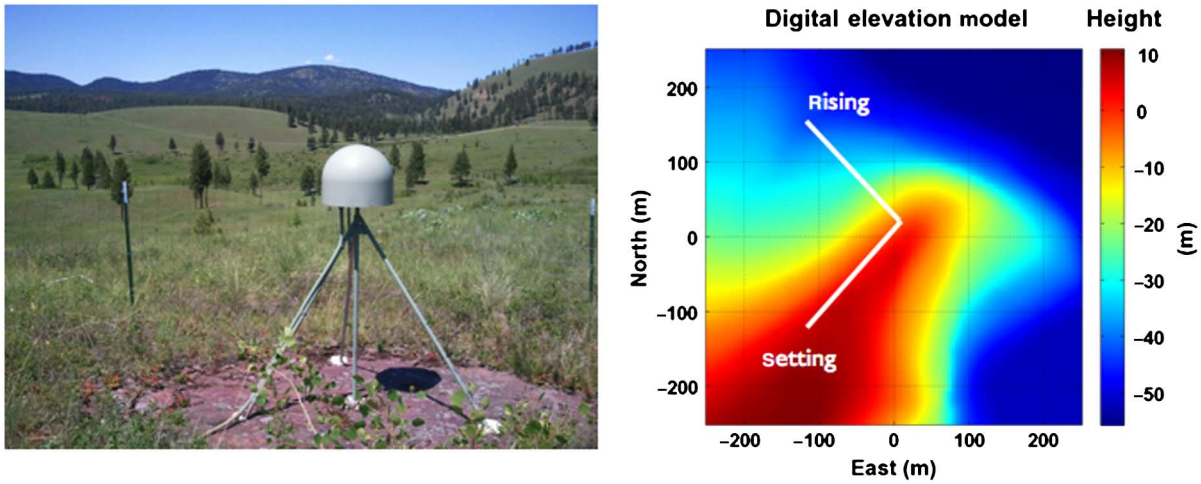

Fig. 3. Left: Typical setup at a continuously operating PBO GPS site in western Montana. The antenna (covered by an acrylic dome) is set atop a tripod monument that has been drilled into the ground. A solar panel (and a bank of batteries) is used to provide power for the system; right: digital elevation map (DEM) for site P048. The ground track for satellite 1 is shown in white.

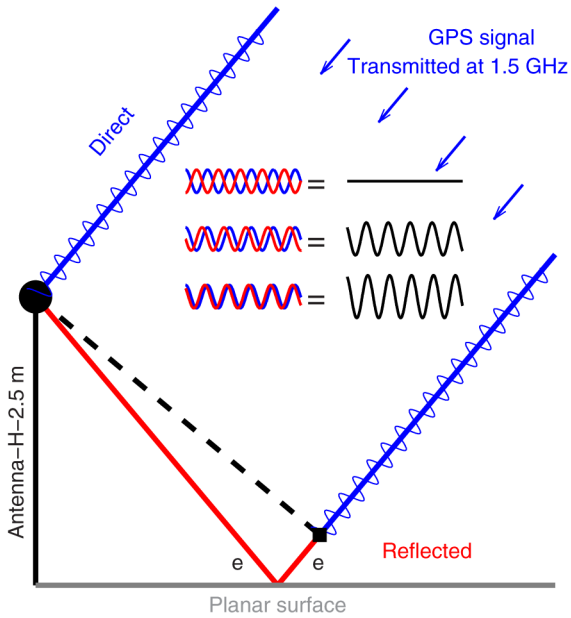

Fig. 4. Each GPS satellite transmits a signal that arrives at an individual receiver on the Earth as a plane wave. A planar reflector is shown in gray. The antenna is 2.5 m above the reflecting surface and represented by the black circle. The direct signal (blue) travels a shorter distance than the reflected signal (blue plus red). The elevation angle of the satellite with respect to the horizon is e. The GPS carrier signal (wavelength ~ 19 cm) is shown superposed on the direct signal. Depending on the extra path travelled by the reflection (shown in red), the direct and reflected signals will interfere (shown for three examples in the center of the figure). This interference (shown in black) is what is measured by the GPS unit.

To determine the phase of the interference pattern, we first calculate the excess path delay D generated by the reflection. Fig. 4 shows the geometric representations of both the direct and the reflected signals. For a horizontal planar reflector, it can be shown that D is

$$D = 2H \sin e \tag{1}$$

where H is the height of the antenna above the reflecting surface and e is the elevation angle of the satellite with respect to the horizon [44]. The phase φ_1 of the interference for a GPS carrier wavelength λ_1 is then

$$\varphi_1 = \frac{2\pi}{\lambda_1} D = \frac{4\pi H}{\lambda_1} \sin e. \tag{2}$$

The frequency of the interference (also known as its modulation) is the time derivative of the phase

$$\frac{d\varphi_1}{dt} = \frac{d}{dt}\left(\frac{4\pi H}{\lambda_1} \sin e\right) = \frac{2\pi}{\lambda_1} 2\mathrm{H} \cos e \frac{de}{dt}. \tag{3}$$

Equation (3) shows that the interferometric frequency will be greater for large H than small H, and will change as the satellite rises (or sets).

A full derivation of multipath effects on GPS signals is beyond the scope of this paper. A short summary is provided in Appendix I. Pseudorange multipath error on the L1 frequency (M_1) depends directly on excess path length D and is defined as

$$M_1 = \frac{\alpha \mathrm{D} \cos \varphi_1}{1 + \alpha \cos \varphi_1} \tag{4}$$

where α is a damping factor defined as the ratio between the reflected (multipath) amplitude (A_m) and the direct signal amplitude (A_d).

Both A_m and A_d depend strongly on elevation angle. The direct signal term A_d is mostly controlled by the antenna gain. It has several key characteristics in a geodetic GPS instrument:

1) The antenna gain for RHCP is many orders of magnitudes stronger than for LHCP.
2) The antenna trades off tracking higher elevation satellites at the expense of lower elevation satellites; therefore A_d is smaller at low elevations than high elevations.
3) A_d depends on transmission power levels. However, this effect is much smaller than the antenna gain effect.

The reflection characteristics of the surface are encompassed in A_m. This is the parameter that is sensitive to VWC: higher VWC leads to lower A_m. For the choke ring antenna used by the

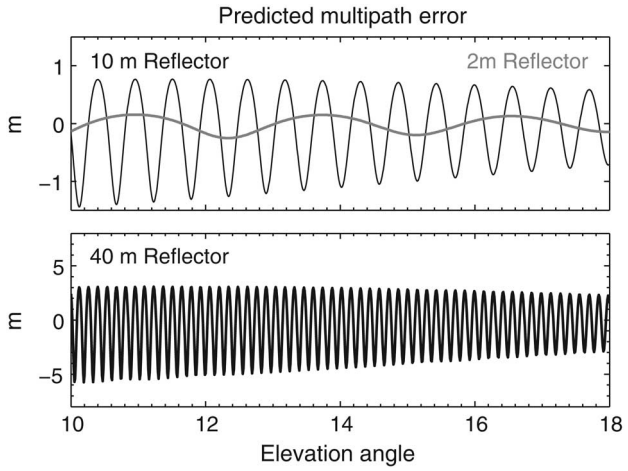

Fig. 5. Predicted multipath errors for planar, horizontal reflectors at three vertical distances: 2, 10, and 40 m. Note the change in vertical scale. The α profile used for the predictions was chosen to be consistent with GPS observations using PBO instrumentation, i.e., it exponentially decays as elevation angle increases.

PBO network [and using (4)], one can predict the general characteristics of pseudorange multipath errors. Fig. 5 shows multipath predictions for antennas at three different heights above a horizontal planar reflector. We can see that the dominant frequency in multipath errors depends directly on the height of the antenna above the reflecting surface (H), i.e., "far" reflectors have high frequencies and vice versa. Secondly, the amplitude of multipath also depends strongly on H, so that far reflectors have much larger amplitudes than near reflectors.

These multipath predictions shown in Fig. 5 are very simplified in the sense that the model uses a generic representation of α and because only a simple planar reflecting surface was used. To fully model GPS multipath errors, the actual reflection coefficients of the surface must be known (e.g., bare soil, surface roughness, soil type and wetness, and characterization of the vegetation), the gain of the antenna for both RHCP and LHCP must be defined, and the terrain surrounding the antenna must be modeled. A simulator to make these types of model predictions is under development, with initial efforts focusing on simple geometries and bare soil [50]–[52]. At the current time, we use the simple principles outlined in Section III to help us define a GPS multipath metric (NMRI) that is sensitive to VWC. In Section IV, we define how GPS pseudorange multipath can be observed.

IV. GPS Multipath: Observations

A. Observable Equations

There are two kinds of GPS observables: pseudoranges and carrier phases (carrier phase is *not* the same as the interferometric phase discussed in Section III). We first define the L_1 ranging observable P_1 (pseudorange). For a given receiver and satellite and time, P_1 is defined as

$$P_1 = \rho + c\delta_r - c\delta_s + I/f_1^2 + T + M_1 + \varepsilon_1. \tag{5}$$

The terms that depend on the transmit frequency have subscripts of 1 for the L_1 frequency. The geometric range term ρ represents the path traveled by the signal from the satellite to the receiver in a vacuum (i.e., the straight-line path). For a GPS receiver on the Earth, this term varies from $\sim 22\,000 - 25\,000$ km. δ represents clock errors for either the receiver or satellite; it is scaled by the speed of light, c. Clock errors can easily produce error terms greater than 100 km. (Note: relativistic effects have been subsumed into the satellite clock term.) The ionospheric delay term (I) depends on how many electrons are along the path between the satellite and receiver and is scaled by the inverse square of the transmit frequency. The tropospheric delay T (gases and precipitable water vapor) also depends on the path between the receiver and the satellite; however, it is not frequency-dependent at GPS frequencies. For convenience, the frequency-scaled ionospheric and tropospheric error terms are shown as having units of meters. The measurement error term is shown as ε_1. M_1 is the pseudorange multipath term described in Section III and the parameter of interest in this study. We must remove as many terms as possible from (5) in order to isolate M_1. Although not used in this paper, we note that there is a pseudorange observable on the L_2 frequency.

The codes (used to define the pseudoranges) are transmitted on carrier signals. The phases of these carrier signals can be converted into very precise, biased ranges. The carrier phase observables (ϕ_1 and ϕ_2) are very similar to P_1:

$$\lambda_1\phi_1 = \rho + c\delta_r - c\delta_s - I/f_1^2 + T + m_1 + N_1\lambda_1 + \varepsilon_\phi \tag{6}$$

$$\lambda_2\phi_2 = \rho + c\delta_r - c\delta_s - I/f_2^2 + T + m_2 + N_2\lambda_2 + \varepsilon_\phi. \tag{7}$$

where N_1 and N_2 are known as carrier phase ambiguities. These must be estimated for positioning applications. The terms can change due to "cycle slips" or "loss of lock," meaning new values must be estimated. To mitigate their impact, only data above elevation angles above 10° are used in this study. The measurement error term for carrier phase (ε_ϕ) is several millimeters and much smaller than that of pseudorange ($\varepsilon_1 \sim 25 - 30$ cm). Note that the ionospheric error for carrier phase data has the opposite sign as for pseudorange. Carrier phase multipath errors (m_1 and m_2) are bounded to be one quarter of the carrier phase wavelength, ~ 5 cm. The geometric range, clock errors, and tropospheric errors are identical for carrier phase and pseudorange data.

The reader will note that simply subtracting $\lambda_1\varphi_1$ from P_1 would isolate pseudorange multipath, but at the expense of doubling the ionospheric error. If, however, P_1 and both carrier phase observables are used, one can isolate pseudorange multipath and remove the ionospheric error. This observable—MP_1—is frequently used in the geodetic community because it has no dependence on orbits, clocks, or atmospheric delays:

$$MP_1 = P_1 - \frac{f_1^2 + f_2^2}{f_1^2 - f_2^2}\lambda_1\phi_1 + \frac{2f_2^2}{f_1^2 - f_2^2}\lambda_2\phi_2 = M_1 + C + \varepsilon_1. \tag{8}$$

C is a scaled linear combination of the carrier phase biases. As long as there are no cycle slips, C is a constant bias and of no intrinsic interest. In future discussion, it will be assumed that a mean value has been removed from computed values of MP_1.

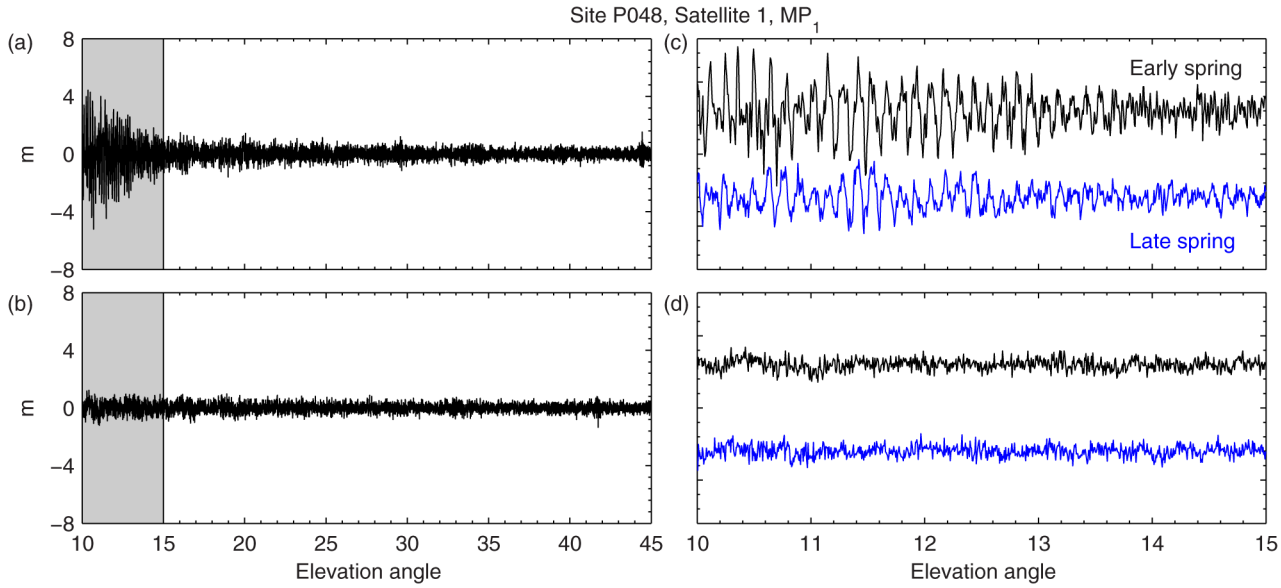

Fig. 6. MP_1 data for site P048 and satellite 1: (a) rising arc (northwest azimuths), (b) setting arc (southwest azimuths), (c) lowest elevation angle data from panel A (shown in gray), (d) lowest elevation angle data from panel (b). Data in (c) and (d) are vertically offset to show data from both late (blue) and early (black) spring.

Note also that ε_ϕ and the carrier phase multipath terms have been dropped. This is because they are 1–2 orders of magnitude smaller than the equivalent pseudorange terms.

B. *Example of* MP_1 *for One Satellite Track*

Equations (5)–(7) are defined at the time a GPS signal is received on the Earth. For any given GPS receiver that records measurements every 15 s, there are thousands of MP_1 measurements per day per satellite. We use the satellite track highlighted in Fig. 1 to demonstrate some of the features of MP_1 data (Fig. 6). The satellite rises in the northwest and sets in the southwest several hours later; we split it into a northwest track and a southwest track [Fig. 6(a) and (b)]. For elevation angles greater than 20°, the MP_1 time series for this satellite track is dominated by a white noise process, with a somewhat larger RMS in the northwest than in the southwest portion. There is no obvious evidence of the multipath effects that were shown in Section IV. However, at low elevation angles [Fig. 6(c)], the northwest track is dominated by high-frequency, high-amplitude oscillations. These observations are consistent with multipath predictions for a reflector height of ~ 40 m (Fig. 5, bottom panel). In contrast, at best there is only a weak multipath signal as the satellite sets in the southwest [Fig. 6(d)]. Since the same satellite transmitted the signal (satellite 1) and the same receiver (P048) recorded the data, the source of the difference must be related to the terrain at the site. Recall, that it is geometry (i.e., reflector heights) that controls pseudorange multipath frequencies, not vegetation. The latter only impacts pseuodorange multipath amplitudes.

The digital elevation map (Fig. 3) for P048 provides insight as to the source of the differences. P048 site is located on a hill. To the northwest, there is a flattening in the terrain ~ 100 m from the antenna. This region is locally planar and ~ 40 m below the antenna. In contrast, reflections from satellites rising/setting in the northeast, at the same elevation angles ($10^\circ - 15^\circ$) and at the elevation difference, are not observed. This is because the hill blocks the antenna from receiving the far reflections from the northeast.

In contrast, the terrain to the southwest has a fairly gentle slope. Forward models using the DEM for this site indicate that the terrain southwest of the antenna is consistent with a nominal reflector height of ~ 2 m [51]. We can also see in Fig. 6(c) that the amplitude of the MP_1 oscillations is significantly smaller in the late spring than was observed in early spring. Since we know that GPS has a repeating ground track (Section II), this decrease in MP_1 amplitude between early and late spring must be caused by a decrease in the multipath reflection coefficient α. This change is consistent with an increase in VWC between the two dates. The southwest satellite track shows no obvious variation in α between early and late spring because the multipath error is small compared to the measurement error ε_1.

C. *Defining a Multipath Reflection Metric*

We seek a precise GPS reflection metric based on MP_1 that is 1) sensitive to the reflectivity (and thus vegetation cover) of the ground and 2) representative of the vegetation surrounding each site. Since MP_1 time series vary to first order as αD (recall that D is the excess path length), the RMS of an individual MP_1 time series will also depend on αD (accomplishing goal 1). Recalling the expansive azimuthal coverage of the GPS constellation [Fig. 1(a)], an average of the all the satellite MP_1 RMS data fulfills goal 2. A database of daily mean MP_1 RMS statistics for each site is routinely compiled by the operators of PBO [53]; hereafter we will call this statistic $\mathrm{MP}_1\mathrm{rms}$, as in [39]. The $\mathrm{MP}_1\mathrm{rms}$ is a weighted mean, i.e., it is weighted by the number of observations for each satellite.

For an L-band bi-static radar, we expect that $\mathrm{MP}_1\mathrm{rms}$ in western Montana (the location of P048) will be largest in early spring (when vegetation has low water content) and smaller in early summer (when VWC peaks). This hypothesis is supported by the $\mathrm{MP}_1\mathrm{rms}$ observations [Fig. 7(a)]. The individual satellite

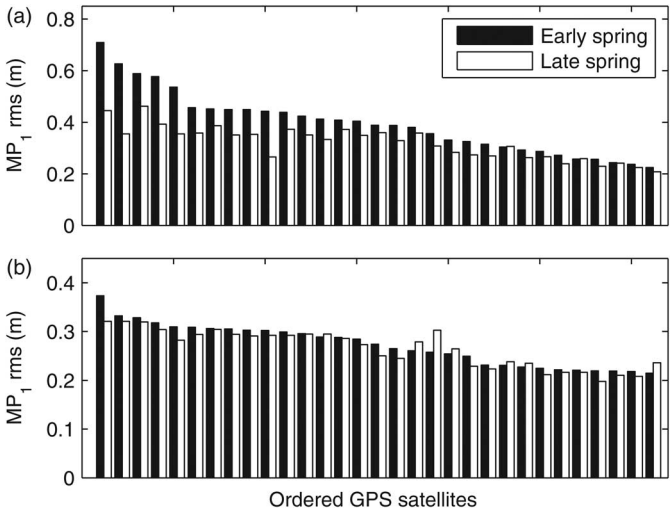

Fig. 7. (a) Station P048 MP1rms (ordered by magnitude) for individual GPS satellites for days in early and late spring and (b) the same quantities for station P041, near Boulder, Colorado. GPS satellites are numbered from 1 to 31.

$\mathrm{MP_1rms}$ data also show the effects of terrain. Satellites 30, 10, 4, 5, and 29 [shown furthest to the left in Fig. 7(a)] all have very large $\mathrm{MP_1rms}$ values. These satellites also have the largest percentage of satellite observations from the northwest azimuths [i.e., Fig. 6(a)].

Even though it is difficult to see any kind of multipath effect in the individual $\mathrm{MP_1rms}$ time series at flatter sites, we have still found it possible to detect seasonal signals by averaging over the entire constellation. PBO site P041, located south of Boulder, Colorado, is a "flat" site. The antenna is 2 m above the ground, and there is less than 20 cm of terrain relief over the nominal GPS footprint. In Fig. 7(b), we plot individual satellite $\mathrm{MP_1rms}$ values for two days, one in early and the other late spring. The seasonal variations are not nearly as striking as they were for P048. For a few satellites, the ground is more reflective in late spring than early spring (e.g., satellite 24). But overall, there are many more that follow the expected behavior of VWC, high $\mathrm{MP_1rms}$ in early spring and low $\mathrm{MP_1rms}$ in late spring. We have found that by using averages of the individual satellite $\mathrm{MP_1rms}$ time series, vegetation signals are detectable at more than 300 PBO sites. Before these $\mathrm{MP_1rms}$ data can be used for phenological studies, we must first address the issue of outliers caused by snow and rain.

D. Outlier Detection

A typical time series of daily $\mathrm{MP_1rms}$ values is shown in Fig. 8(a). The 6-year $\mathrm{MP_1rms}$ time series shows similar behavior as 16-day NDVI data [Fig. 8(d)]. However, there is significant scatter in the winter and late fall that appears to be more episodic in nature. Many—but not all—of these outliers are coincident with near-zero NDVI values, i.e., they are consistent with snow cover.

Because GPS is an L-band system, GPS reflections will be sensitive to water within and on the surface of vegetation, as well as water in soil and snow. It is this very sensitivity that is being used by other terrestrial hydrology investigators [26], [27], [36]–[38], [53]–[55]. To isolate the vegetation signal,

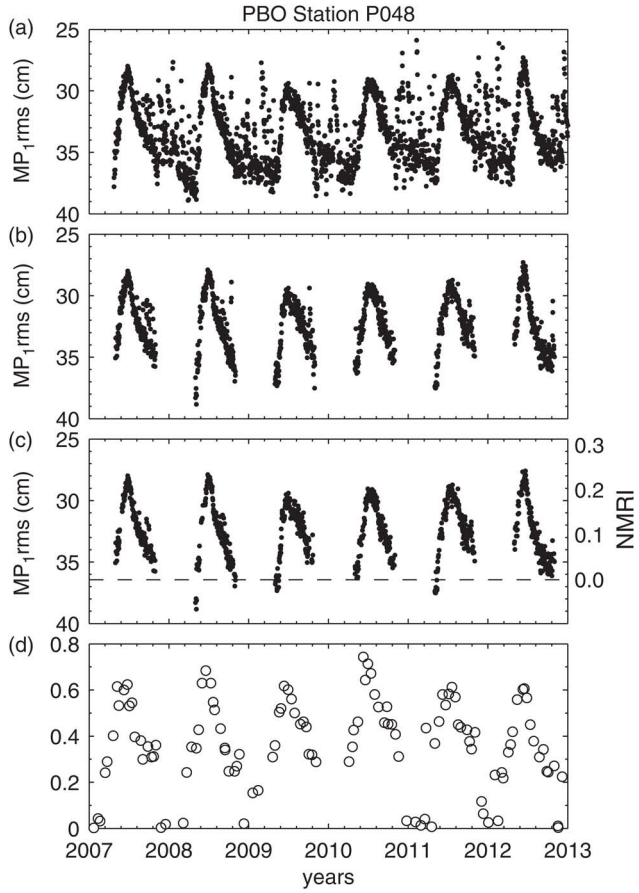

Fig. 8. (a) $\mathrm{MP_1rms}$ values for station P048 taken from the UNAVCO database [53] (observed), (b) $\mathrm{MP_1rms}$ data after snow clearing using climatology model, (c) final edited $\mathrm{MP_1rms}$ time series, with NMRI values shown on the right y-axis, and (d) 16-day MODIS NDVI product.

$\mathrm{MP_1rms}$ data impacted by snow and very wet soil must be removed. We used the [56] dataset of climatological monthly snow water equivalent to identify times when snow was likely; data from those months were removed [Fig. 8(b)]. This is an overly conservative data editor; an improved snow filter is being developed that uses measured snow-extent observations from MODIS. The remaining outliers in the $\mathrm{MP_1rms}$ data are mostly related to early or late snowstorms or rainfall. Modeled temperature and precipitation data from the North American Land Data Assimilation System (NLDAS) were used to identify these early/late snowfall events and rainfall [57]. Snow events were defined based on the minimum NLDAS temperature and the daily precipitation value being greater than 2 mm. For small rain events (5–10 mm), that day was removed. For larger rain events (>10 mm), both the day it rained and the following day were removed. Finally, a 2-week running mean was used to identify and remove three-standard deviation outliers. The resulting $\mathrm{MP_1rms}$ data are shown in Fig. 8(c).

E. Normalization

The $\mathrm{MP_1rms}$ results for site P048 shown in Fig. 7(c) are consistent with those presented by [39], although the time series is now 6 years long instead of 3 years. Outliers present in that initial study are now much less frequent. Changes in NDVI strongly correlate (~ -0.8) with changes in $\mathrm{MP_1rms}$ at P048

[Fig. 8(d)]. This is the case at many other PBO sites, although $\mathrm{MP_1rms}$ changes in the P048 eco-region typically lag those observed in NDVI by 1–3 weeks. Since the $\mathrm{MP_1rms}$ values are influenced by the excess path length term D in (4), $\mathrm{MP_1rms}$ time series from different GPS sites cannot be directly compared with each other. For example, at a flat site (P041), the largest $\mathrm{MP_1rms}$ values are ~ 0.28 m; at the hilly site, P048, the largest values are ~ 0.37 m. This does not mean that P048 has VWC that is 32% (the ratio of 0.37/0.28) larger than for P041. In order to remove the first-order terrain effect caused by the excess path delay, we use a normalization (NMRI) that scales $\mathrm{MP_1rms}$ by its maximum value. The latter represents the best estimate of when the signal is being reflected by the land surface with the minimum amount of VWC. In Fig. 8(c), the maximum $\mathrm{MP_1rms}$ (shown by the dashed line) is based on the average of the largest 5% daily $\mathrm{MP_1rms}$ values. A negative ratio is used so that NMRI follows the vegetation growth cycle, i.e., NMRI increases as VWC increases and vice versa:

$$NMRI = \frac{-(MP_1\mathrm{rms} - \max(MP_1\mathrm{rms}))}{\max(MP_1\mathrm{rms})} \tag{9}$$

In paper II, we show that this normalization yields a consistent relationship between NMRI and *in situ* measured VWC across four GPS sites in Montana.

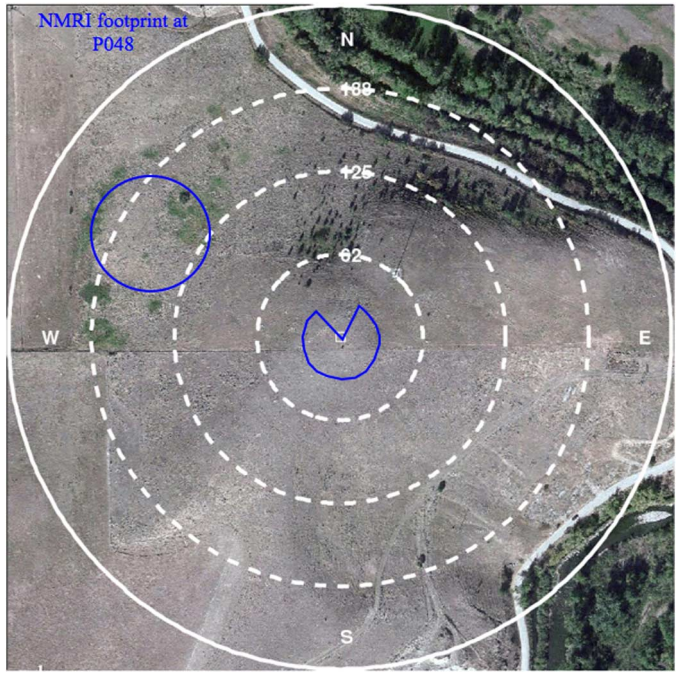

Fig. 9. Footprint of the NMRI metric at GPS site P048. This site's footprint includes both near-reflections (central circle with pie shape removed) based on the $\sim$2-m antenna height and a large secondary footprint (hotspot) to the northwest caused by terrain differences. Image taken from Google Earth. Radial distances given in meters (62, 125, 168, 250) for the white circles.

F. Footprint

Ordinarily the footprint of a remote sensing technique would be described before showing results using the technique. Here, we have first developed simple theoretical descriptions of the method and showed representative results so that the footprint would be seen in that context. If all GPS sites were located in flat terrain, it would be straightforward to define the NMRI footprint (see, e.g., the appendix of [58]). The Fresnel zone for a single rising or setting satellite track (for a typical antenna height) is an ellipse, ~ 22 m in length (starting close to the antenna), but quite narrow (~ 4 m from side to side). By using the entire constellation, the flat-terrain footprint basically mimics the first satellite coverage plot we showed (see Fig. 9). The pie-shaped region removed from the footprint represents the lack of satellites transmitting from the azimuth angles $-30°$ to $30°$. The radius of this site footprint (~ 22 m) depends directly on the antenna height H, $\sim 2 * \mathrm{H}/\tan(\mathrm{e})$, where e is the minimum elevation angle of $10°$ and H is here assumed to be 2 m. The area of the flat-terrain footprint is ~ 1000 m^2. If the GPS antenna was deployed on a 10 m tower over flat terrain, the site footprint would have a radius of ~ 115 m and a correspondingly larger footprint area. However, there are no such tower-mounted sites in the PBO network (Fig. 2).

What about a site like P048, where we know that there are reflections coming in a vertical distance greater than 2 m? We have used a modified version of [51] to calculate the footprint of reflections for P048 using the digital elevation map (Fig. 3). In addition to the central footprint already discussed, this simulation shows a large circular footprint ~ 150 m away from the antenna. The area of this "hotspot" is in fact larger than the central footprint. The NMRI measurement thus includes the effects of both reflection areas, but is dominated by the far reflections. This means that each NMRI site will have its own footprint. For example, at some GPS sites, there will be hotspots to the east of the GPS antenna and at other GPS sites they will be to the south. Some GPS sites will have more than one hotspot. The location and size of the hotspot(s) depend on the vertical height of the planar surface with respect to the antenna. It will also depend on whether these local planar surfaces produce reflections that can be observed at the antenna. These hotspots are most easily mapped out with an electromagnetic simulation software. Such an analysis requires a DEM. Because of the way a GPS receiver's tracking loop has been programmed, no reflected signals can be observed that are delayed more than 300 m. Therefore, the maximum distance of reflections contributing to NMRI is 300 m from the antenna. Thus unlike a satellite remote sensing system, NMRI does not have one pixel size. It has a variable footprint that will yield useful phenological metrics if the footprint is representative of the ecosystem surrounding the antenna. An initial study of 305 NMRI time series found significant correlations with VOD estimates at 90% of the sites, suggesting that the PBO network does have sensing zones that are representative of the regional ecosystems [58].

V. Discussion

Reflected signals measured by GPS ground receivers sense variations that are consistent with vegetation growth. These GPS reflection measurements are calculated on a daily basis and are unaffected by atmospheric effects such as clouds. The spatial footprint of the method depends on the terrain at the site, with a

minimum footprint of $1000\ \mathrm{m}^2$. Methods have been developed to remove errors caused by snow and rain. A preliminary NMRI database has been compiled and consists of $\sim$330 time series spanning the years 2007–2012 (http://xenon.colorado.edu/portal). A landcover classification is provided for each site. The bulk of the sites are grasslands, shrublands, and savannas (146, 74, and 70 sites, respectively). Since the purpose of the GPS network was to precisely measure the position of the ground, very few of the NMRI sites are located in heavily forested regions, as trees degrade positioning accuracy. It is expected that PBO will be maintained by NSF until at least 2020, providing an opportunity to measure the vegetation response to climate variability in the western United States over $\sim$15 years. We plan to add NMRI data for $\sim$50 more sites to the data portal, with most of the new sites coming from desert ecosystems and Alaska. Surface soil moisture content and snow depth are provided for $\sim$150 GPS sites using related GPS reflection methods [54], [55].

Here we have not linked the observed fluctuations in NMRI to changes in any particular biophysical parameters. In paper II, we show that NMRI correlates with VWC measured *in situ* at four sites and correlates strongly with NDVI at 12 sites. All these comparison sites are located in Montana grasslands.

We make five final observations about NMRI:

1) NMRI is based on average $\mathrm{MP_1rms}$ records for each GPS satellite. Other normalizations, such as azimuthally binned $\mathrm{MP_1rms}$ data, should also be examined.
2) The algorithm to remove snow-contaminated values is conservative, which results in significant data removal during the winter. The definition of maximum $\mathrm{MP_1rms}$ can be improved by using satellite products to determine snow cover instead of climatology models.
3) NMRI is sensitive to variations of α from the multipath equation (4). It is not expected that α will directly relate to VWC exactly the same way for different vegetation types. Models for electromagnetic scattering for different vegetation structures should be examined to aid in future normalizations [59].
4) All pseudorange data recorded by geodetic GPS receivers are impacted by multipath reflections. That being said, studies should be undertaken to compare pseudorange multipath recorded by different receiver manufacturers in order to evaluate the possibility of receiver-dependent biases.
5) GPS reflections are impacted by both soil moisture and vegetation growth. We are able to reliably remove the effects of soil moisture in this study because it has a smaller effect on the pseudorange observables than vegetation growth.

VI. Conclusions

The EarthScope PBO was designed and deployed to measure deformation caused by tectonic forces. Here we have shown that these same GPS instruments are sensitive to changes in vegetation state. There are over 10 000 GPS receivers around the world providing data to public archives. Although some of these GPS sites are located in urban areas, many could provide invaluable data for phenological research at very low cost. However, the locations of these sites will always be determined by the primary operator of the network. In the example used in this paper, the site selection was directed by geophysicists. The GPS technology used in this study is commercially available and can be installed by investigators at individual ecosystem study areas, but it would be more useful for phenology if the GPS antennas were deployed on towers. This would provide a large, homogeneous footprint for phenology studies and would complement satellite methods. Since many scientists use differential GPS to locate field sites, such a tower-mounted GPS site could also serve as a base station.

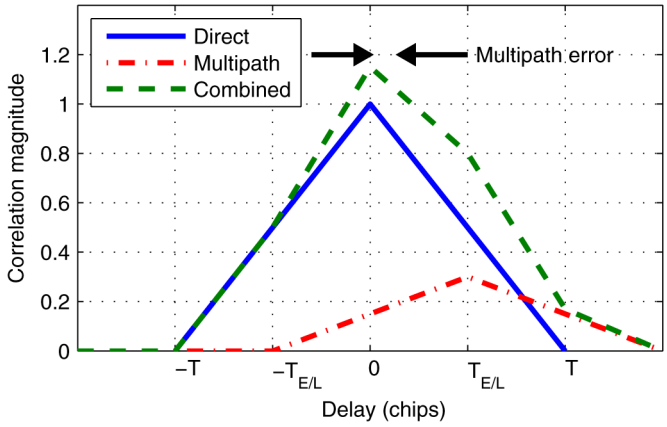

Fig. 10. Cartoon depiction of how multipath impacts the observed pseudorange measurement. The x-axis is measured in chips. The direct signal has no multipath. A single multipath reflection (0.5 chip delay and a relative amplitude of 0.3) is shown in red. The receiver tracks the combined signal (green). The y-axis is the normalized correlation function.

Appendix I

Excellent summaries and discussions about the GPS pseudorange observable and multipath effects can be found in [45]–[47]. Here we follow the descriptions provided by [48], [49]. The pseudorange multipath error (M) is directly related to the code tracking loop behavior and its discriminator equation. In brief, a GPS receiver "tracks" by driving the difference between the early and late discriminator spacing ($2T_{E/L}$) to zero. When no multipath is present (direct only, Fig. 10):

$$R\left(T_{E/L}\right) - R\left(-T_{E/L}\right) = 0 \tag{A1}$$

where R represents the autocorrelation function of the code. However, multipath distorts the correlation function as the receiver must now track the composite signal (combined, Fig. 10) while retaining correlator spacing $2T_{E/L}$. This results in shifted correlator values due to the multipath delay, and a new discriminator equation

$$\begin{aligned}&\left[R\left(M + T_{E/L}\right) - R\left(M - T_{E/L}\right)\right] \\ &\quad + \alpha \cos\varphi\left[R\left(M + T_{E/L} - D\right) - R\left(M - T_{E/L} - D\right)\right] = 0\end{aligned} \tag{A2}$$

where α is the ratio of the of the amplitudes of the reflected and direct signals, φ is the phase shift of the reflected relative to the direct signal, and D is the path delay. If we assume that the

autocorrelation function has an ideal triangular shape for multipath delays shorter than the chip length T

$$R(\tau) = 1 - \frac{|\tau|}{T}, \quad for\ |\tau| < T. \tag{A3}$$

We can reduce (A2) to

$$\frac{-2M}{T} + \alpha \cos\varphi \left(-2\frac{(M-D)}{T} \right) = 0 \tag{A4}$$

and subsequently

$$M = \frac{\alpha D \cos\varphi}{1 + \alpha \cos\varphi}. \tag{A5}$$

Acknowledgments

The authors would like to thank L. Estey, F. Boler, and K. Feaux. J. Braun, F. Nievinski, E. Gutmann, J. Pratt, A. Bilich, and P. Vikram at UNAVCO provided assistance for this project. Some of this material is based on data, equipment, and engineering services provided by the Plate Boundary Observatory operated by UNAVCO for EarthScope and supported by the National Science Foundation (EAR-0350028 and EAR-0732947). All GPS data used in this study are archived at UNAVCO. NMRI time series can be downloaded from http://xenon.colorado.edu/portal.

References

[1] P. Kramer and J. Boyer, *Water Relations of Plants and Soils.* San Diego, CA, USA: Academic Press, 1995, p. 495.

[2] S. L. Ustin, D. A. Roberts, and J. Pinzón, "Estimating canopy water content of chaparral shrubs using optical methods," *Remote Sens. Environ.*, vol. 65, no. 3, pp. 280–291, 1998.

[3] E. G. Njoku and S. K. Chan, "Vegetation and surface roughness effects on AMSR-E land observations," *Remote Sens. Environ.*, vol. 100, no. 2, pp. 190–199, 2006.

[4] D. Entekhabi *et al.*, "The soil moisture active passive (SMAP) mission," *Proc. IEEE*, vol. 98, no. 5, pp. 704–716, May 2010.

[5] C. J. Tucker, "Red and photographic infrared linear combinations for monitoring vegetation," *Remote Sens. Environ.*, vol. 8, no. 2, pp. 127–150, 1979.

[6] A. R. Huete, "A soil adjusted vegetation index (SAVI)," *Remote Sens. Environ.*, vol. 25, no. 3, pp. 295–309, 1988.

[7] G. Gutman and A. Ignatov, "The derivation of the green vegetation fraction from NOAA/AVHRR data for use in numerical weather prediction models," *Int. J. Remote Sens.*, vol. 19, no. 8, pp. 1533–1543, 1998.

[8] J. M. Paruelo, H. E. Epstein, W. K. Lauenroth, and I. C. Burke, "ANPP estimates from NDVI for the central grassland region of the United States," *Ecology*, vol. 78, no. 3, pp. 953–958, 1997.

[9] B. K. Wylie, D. J. Meyer, L. L. Tieszen, and S. Mannel, "Satellite mapping of surface biophysical parameters at the biome scale over the North American grasslands: A case study," *Remote Sens. Environ.*, vol. 79, no. 2–3, pp. 266–278, 2002.

[10] D. Chen, J. Huang, and J. T. Jackson, "Vegetation water content estimation for corn and soybeans using spectral indices derived from MODIS near- and short-wave infrared bands," *Remote Sens. Environ.*, vol. 98, no. 2–3, pp. 225–236, 2005.

[11] P. Ceccato, S. Flasse, and J. Grégoire, "Designing a spectral index to estimate vegetation water content from remote sensing data: Part 2. Validation and applications," *Remote Sens. Environ.*, vol. 82, no. 2–3, pp. 198–207, 2002.

[12] B. Gao, "NDWI-A normalized difference water index for remote sensing of vegetation liquid water from space," *Remote Sens. Environ.*, vol. 58, pp. 257–266, 1996.

[13] L. Serrano, S. L. Ustin, D. A. Roberts, J. A. Gamon, and J. Peñuelas, "Deriving water content of chaparral vegetation from AVIRIS data," *Remote Sens. Environ.*, vol. 74, no. 3, pp. 570–581, 2000.

[14] P. Ceccato, N. Gobron, S. Flasse, B. Pinty, and S. Tarantola, "Designing a spectral index to estimate vegetation water content from remote sensing data: Part 1: Theoretical approach," *Remote Sens. Environ.*, vol. 82, no. 2–3, pp. 188–197, 2002.

[15] T. J. Jackson, D. Chen, M. Cosh, F. Li, M. Anderson, C. Walthall, P. Doriaswamy, and E. R. Hunt, "Vegetation water content mapping using Landsat data derived normalized difference water index for corn and soybeans," *Remote Sens. Environ.*, vol. 92, no. 4, pp. 475–482, 2004.

[16] F. T. Ulaby, T. R. Moore, and A. K. Fung, *Microwave Remote Sensing: Active and Passive, From Theory to Applications*, vol. III. Norwood, MA, USA: Artech House, 1981.

[17] T. J. Jackson and T. J. Schmugge, "Vegetation effects on the microwave emission of soils," *Remote Sens. Environ.*, vol. 36, pp. 203–212, 1991.

[18] M. O. Jones, J. S. Kimball, E. E. Small, and K. M. Larson, "Comparing land surface phenology derived from satellite and GPS network microwave remote sensing," *Int. J. Biometeorol.,* 2013, doi: 10.1007/s00484-013-0726-z.

[19] T. W. Brakke, E. T. Kanemasu, J. L. Steiner, F. T. Ulaby, and E. Wilson, "Microwave radar response to canopy moisture, leaf area index, and dry weight of wheat, corn, and sorghum," *Remote Sens. Environ.*, vol. 11, pp. 207–220, 1981.

[20] M. J. Hill, G. E. Donald, and P. J. Vickery, "Relating radar backscatter to biophysical properties of temperate perennial grassland," *Remote Sens. Environ.*, vol. 67, no. 1, pp. 15–31, 1999.

[21] S. Paloscia, G. Macelloni, P. Pampaloni, and E. Santi, "The contribution of multitemporal SAR data in assessing hydrological parameters," *IEEE Geosci. Remote Sens. Lett.*, vol. 1, no. 3, pp. 201–205, Jul. 2004.

[22] R. D. De Roo, F. T. Ulaby, and M. C. Dobson, "A semi-empirical backscattering model at L-band and C-band for a soybean canopy with soil moisture inversion," *IEEE Trans. Geosci. Remote Sens.*, vol. 39, no. 4, pp. 864–872, Apr. 2001.

[23] Y. Kim, J. T. Jackson, R. Bindlish, H. Lee, and S. Hong, "Radar vegetation indices for estimating the vegetation water content of rice and soybean," *IEEE Geosci. Remote Sens. Lett.*, vol. 9, no. 4, pp. 564–568, Jul. 2012.

[24] Y. Kim and J. J. van Zyl, "A time-series approach to estimate soil moisture using polarimetric radar data," *IEEE Trans. Geosci. Remote Sens.*, vol. 47, no. 8, pp. 2519–2527, Aug. 2009.

[25] M. Martin-Neira, "A passive reflectometry and interferometry system (PARIS): Application to ocean altimetry," *ESA J.*, vol. 17, pp. 331–355, 1993.

[26] D. Masters, P. Axelrad, and S. Katzberg, "Initial results of land-reflected GPS bistatic radar measurements in SMEX02," *Remote Sens. Environ.*, vol. 92, no. 4, pp. 507–520, 2002.

[27] S. Katzberg, O. Torres, M. Grant, and D. Masters, "Utilizing calibrated GPS reflected signals to estimate soil reflectivity and dielectric constant: Results from SMEX02," *Remote Sens. Environ.*, vol. 100, no. 1, pp. 17–28, 2006.

[28] S. T. Lowe, C. Zuffada, Y. Chao, P. Kroger, L. E. Young, and J. L. LaBrecque, "5-cm-precision aircraft ocean altimetry using GPS reflections," *Geophys. Res. Lett.*, vol. 29, no. 10, 2002.

[29] H. Carreno-Luengo, H. Park, A. Camps, F. Fabra, and A. Rius, "GNSS-R derived centimetric sea topography: An airborne experiment demonstration," *IEEE J. Sel. Topics Appl. Earth Observ.*, vol. 6, no. 3, pp. 1468–1478, Jun. 2013.

[30] J. L. Garrison, A. Komjathy, V. U. Zavorotny, and S. J. Katzberg, "Wind speed measurement using forward scattered GPS signals," *IEEE Trans. Geosci. Remote Sens.*, vol. 40, no. 1, pp. 50–65, Jan. 2002.

[31] A. Komjathy, J. A. Maslanik, V. U. Zavorotny, P. Axelrad, and S. J. Katzberg, "Sea ice remote sensing using surface reflected GPS signals," in *Proc. IEEE Int. Geosci. Remote Sens. Symp.* (IGARSS 2000), Honolulu, HI, USA, Jul. 24–28, 2000, pp. 2855–2857.

[32] E. Valencia, A. Camps, N. Rodriguez-Alvarez, H. Park, and I. Ramos-Perez, "Using GNSS-R imaging of the ocean surface for oil slick detection," *IEEE J. Sel. Topics Appl. Earth Observ.*, vol. 6, no. 1, pp. 217–223, Feb. 2013.

[33] M. Semmling, G. Beyerle, R. Stosius, G. Dick, J. Wickert, F. Fabra, E. Cardellach, S. Ribó, A. Rius, and A. Helm, "Detection of arctic ocean tides using interferometric GNSS-R signals," *Geophys. Res. Lett.*, vol. 38, no. 4, 2011.

[34] K. M. Larson, R. Ray, F. Nievinski, and J. Freymueller, "The accidental tide gauge: A case study of GPS reflections from Kachemak Bay, Alaska," *IEEE Geosci. Remote Sens. Mag.*, vol. 10, no. 5, pp. 1200–1205, Sep. 2013.

[35] E. Cardellach, F. Fabra, A. Rius, S. Pettinato, and S. D'Addio, "characterization of dry-snow sub-structure using GNSS reflected signals," *Remote Sens. Environ.*, vol. 124, no. 9, pp. 122–134, 2012.

[36] N. Rodriguez-Alvarez, A. Camps, M. Vall-Ilossera, X. Bosch-Lluis, A. Monerris, I. Ramos-Perez *et al.*, "Land geophysical parameters retrieval using the interference pattern GNSS-R technique," *IEEE Trans. Geosci. Remote Sens.*, vol. 49, no. 1, pp. 71–84, Jan. 2011.

[37] N. Rodriguez-Alvarez, X. Bosch-Lluis, A. Camps, A. Aguasca, M. Vall-Illossera, E. Valencia, I. Ramos-Perez, and H. Park, "Review of crop growth and soil moisture monitoring from a ground-based instrument implementing the interference pattern GNSS-R technique," *Radio Sci.*, vol. 46, no. 6, 2011.
[38] A. Egido, M. Caparrini, G. Ruffini, S. Paloscia, L. Guerriero, N. Pierdicca, and N. Floury, "Global navigation satellite system reflectometry as a remote sensing tool for agriculture," *Remote Sens.*, vol. 4, no. 8, pp. 2356–2372, 2012.
[39] E. E. Small, K. M. Larson, and J. J. Braun, "Sensing vegetation growth with GPS reflections," *Geophys. Res. Lett.*, vol. 37, no. 12, p. L12401, 2010.
[40] E. E. Small, K. M. Larson, and W. Smith, "Normalized microwave reflection index, part II: Validation of vegetation water content estimates using from Montana grasslands," *IEEE J. Sel. Topics Appl. Earth Observ.*, revised.
[41] D. C. Agnew and K. M. Larson, "Finding the repeat times of the GPS constellation," *GPS Solutions*, vol. 11, no. 1, pp. 1–9, 2007.
[42] W. H. Prescott, J. L. Davis, and J. L. Svarc, "Global positioning system measurements for crustal deformation," *Science*, vol. 244, no. 4910, pp. 1337–1339, 1989.
[43] J. M. Tranquilla, J. P. Carr, and H. M. Al-Rizzo, "Analysis of a choke ring groundplane for multipath control in GPS applications," *IEEE Trans. Antennas Propag.*, vol. 42, no. 7, pp. 905–911, Jul. 1994.
[44] Y. Georgiadou and A. Kleusberg, "On carrier signal multipath effects in relative GPS positioning," *Manusc. Geod.*, vol. 13, pp. 172–179, 1988.
[45] P. Misra and P. Enge, *Global Positioning System: Signals, Measurements, and Performance*, revised 2nd ed. Lincoln, MA, USA: Ganga-Jamuna Press, 2011.
[46] M. S. Braasch, "Multipath effects," in *Global Positioning System: Theory and Applications*, vol. 1, B. W. Parkinson, J. J. Spilker Jr., P. Axelrad, and P. Enge, Eds. Washington, DC, USA: AIAA, 1995, pp. 547–568.
[47] J. K. Ray and M. E. Cannon, "Synergy between global positioning system code, carrier, and signal-to-noise ratio multipath errors," *J. Guid. Control Dyn.*, vol. 24, no. 1, pp. 54–63, 2001.
[48] P. Axelrad, K. M. Larson, and B. Jones, "Use of the correct satellite repeat period to characterize and reduce site-specific multipath errors," in *Proc. Inst. Navig.,* Long Beach, CA, USA, 2005, pp. 2638–2648.
[49] A. Bilich, "Improving the Precision and accuracy of geodetic GPS: Applications to multipath and seismology," Ph.D. dissertation, Univ. Colorado, Boulder, CO, USA, 2006.
[50] V. Zavorotny, K. M. Larson, J. J. Braun, E. E. Small, E. Gutmann, and A. Bilich, "A physical model for GPS multipath caused by ground reflections: Toward bare soil moisture retrievals," *IEEE J. Sel. Topics Appl. Earth Observ.*, vol. 3, no. 1, pp. 100–110, Mar. 2010.
[51] F. G. Nievinski and K. M. Larson, "A GPS multipath simulator for near-surface reflectometry and positioning applications," *GPS Solutions,* 2014, doi: 10.1007/s10291-013-0331-y.
[52] C. C. Chew, E. E. Small, K. M. Larson, and V. Zavorotny, "Effects of near-surface soil moisture on GPS SNR data: Development of a retrieval algorithm for volumetric soil moisture," *IEEE Trans. Geosci. Remote Sens.*, vol. 52, no. 1, pp. 537–543, Jan. 2014.
[53] L. Estey and C. Meertens, "TEQC: The multi purpose toolkit for GPS/GLONASS data," *GPS Solutions*, vol. 3, no. 1, pp. 42–49, 1999.
[54] K. M. Larson, E. E. Small, E. Gutmann, A. Bilich, J. Braun, and V. Zavorotny, "Use of GPS receivers as a soil moisture network for water cycle studies," *Geophys. Res. Lett.*, vol. 35, p. L24405, 2008.
[55] K. M. Larson, E. Gutmann, V. Zavorotny, J. Braun, M. Williams, and F. Nievinski, "Can we measure snow depth with GPS receivers?" *Geophys. Res. Lett.*, vol. 36, p. L17502, 2009.
[56] R. L. Armstrong, M. J. Brodzik, K. Knowles, and M. Savoie, *Global Monthly EASE-Grid Snow Water Equivalent Climatology,* Version 1.0. Boulder, CO, USA: National Snow and Ice Data Center, 2007.
[57] K. E. Mitchell *et al.*, "The multi-institution North American Land Data Assimilation System (NLDAS): Utilizing multiple GCIP products and partners in a continental distributed hydrological modeling system," *J. Geophys. Res.*, vol. 109, p. D07S90, 2004.
[58] K. M. Larson and F. G. Nievinski, "GPS snow sensing: Results from the EarthScope plate boundary observatory," *GPS Solutions*, vol. 17, no. 1, pp. 41–52, 2013.
[59] C. C. Chew, E. E. Small, K. M. Larson, and V. Zavorotny, "Utility and limitations of GPS interferometric reflectometry for vegetation sensing," *IEEE Trans. Geosci. Remote Sens.*, accepted for publication.

Kristine M. Larson received the B.A. degree in engineering sciences from Harvard University, Cambridge, MA, USA, in 1985, and the Ph.D. degree in geophysics from the Scripps Institution of Oceanography, University of California, San Diego, La Jolla, CA, USA, in 1990.

She is a Professor with the Department of Aerospace Engineering Sciences, University of Colorado, Boulder, CO, USA. Her research interests are focused on developing new applications and techniques for GPS.

Eric E. Small received the B.A. degree in geological sciences from Williams College, Williamstown, MA, USA, in 1993, and the Ph.D. degree in earth sciences from the University of California, Santa Cruz, CA, USA, in 1998.

He is a Professor with the Department of Geological Sciences, University of Colorado, Boulder, CO, USA. His research is focused on land surface hydrology.